Dual-band flexible terahertz metamaterial sensor based on nested resonant rings

JIANJUN LIU, JIANHUA LONG, SONXI HU*
School of Intelligent Engineering, Shaoguan University, Shaoguan Guangdong, 512005, China

A dual-band terahertz metamaterial sensor based on nested split-ring resonators and closed square rings on a flexible polyimide substrate is proposed in this paper. The structure consists of an outer split-ring resonator, an inner closed square ring, and a continuous gold ground plane. Simulations using CST Studio Suite 2022 demonstrate two independent resonant peaks at 1.107 THz and 1.4414 THz in air, with absorption rates of 99.87% and 99.82%, respectively. The refractive index sensitivity reaches 237.93 GHz/RIU, and the frequency shift exhibits an excellent linear relationship with the refractive index variation. The sensor also features polarization insensitivity and angular stability. Analyses of the electric field, magnetic field, and surface current distributions indicate that the low-frequency mode is primarily excited by the fundamental LC resonance dominated by the outer split ring, while the high-frequency mode arises from the loop-current magnetic resonance dominated by the inner closed square ring. With its simple structure, strong fabrication compatibility, and outstanding robustness, the proposed design simultaneously achieves high absorption, high sensitivity, and comprehensive environmental adaptability on a flexible substrate compared with recent dual-band terahertz sensors. It holds significant potential for biomolecular detection, chemical trace analysis, and wearable sensing applications.

(Received January 26, 2026; accepted June 2, 2026)

Keywords: Terahertz metamaterials, Dual-band absorber, Polarization-insensitive, Angularly stable

1. Introduction

Terahertz (THz) waves, spanning 0.1–10 THz and lying between microwaves and infrared radiation, are non-ionizing and feature low photon energy and strong penetrability. These characteristics endow THz technology with considerable potential in biomedical imaging, chemical substance identification, non-destructive testing, and wireless communications [1-3]. In particular, many biomolecules (e.g., proteins, DNA, and cancer-related tissues) exhibit characteristic vibrational and rotational responses in the THz band, enabling label-free detection with high specificity [4-6]. Nevertheless, the practical deployment of THz systems is still hindered by the high cost and limited sensitivity of conventional THz sources and detectors. As artificially engineered electromagnetic media, metamaterials provide a powerful route to manipulate THz waves through subwavelength resonant unit cells, thereby offering an effective platform for developing high-performance THz absorbers and sensors [7-9].

Metamaterial-based THz sensors typically exploit strong near-field enhancement and sharp resonances to convert subtle variations in the surrounding dielectric environment into measurable spectral shifts, enabling highly sensitive refractive-index sensing [10-12]. Compared with single-frequency structures, multi-/dual-frequency designs can introduce composite resonance modes (e.g., nested or multilayer configurations) to generate multiple relatively independent resonant peaks, supporting multi-channel detection, self-referenced measurement, and multi-analyte identification with improved efficiency and specificity [13-15]0. In recent years, the feasibility of dual-frequency THz metamaterial sensors has been demonstrated in refractive-index sensing, thin-film biomolecule recognition, and gas detection, with sensitivities reaching hundreds of GHz/RIU [16-18]. For example, Yang et al. [1] (2025) combined dual-frequency THz metamaterial sensing with deep learning to improve identification efficiency, while Li et al. [7] (2025) proposed a dual-frequency ring-type metamaterial biosensor with enhanced sensitivity. In addition, a series of recent studies have investigated broadband/multiband THz metamaterial absorbers and absorber–sensor integrated structures, reporting high-absorption performance and tunability enabled by strategies such as Dirac semimetals, graphene-coupled resonances, and multimode excitation, which further enrich the design toolbox and application scenarios of THz absorption and sensing devices [25-28].

Despite these advances, existing multi-frequency THz metamaterial sensors still face several common bottlenecks for practical deployment. First, many designs are highly sensitive to the polarization angle of the incident wave, leading to pronounced differences between TE and TM responses, which limits stable operation in randomly polarized or complex environments [19, 20]. Second, their angular stability is often insufficient: absorption peaks may decay rapidly under oblique incidence (e.g., a notable degradation beyond 40°–50°), which is unfavorable for non-ideal incidence conditions. Third, most high-performance devices rely on rigid substrates (such as silicon or quartz), making it difficult to satisfy the requirements of wearable or conformal applications that demand flexibility and deformation tolerance. Although flexible substrates (e.g., polyimide, PI) offer mechanical compliance, they may be accompanied by reduced Q factors, broadened resonances, or compromised robustness in some reports. For instance, the dual-frequency VO_2-based device reported by Liu et al. [8] (2025) exhibits high sensitivity, yet its rigid implementation restricts flexible applications.

From the perspective of structural design, nesting a split-ring resonator (SRR) with a square ring can excite multimode resonances via the combined response of the inner and outer resonators, providing an effective scheme to achieve dual-frequency operation. Previous studies have shown that such nested configurations can support dual LC modes or loop-current magnetic resonances; however, most demonstrations are still based on rigid substrates and exhibit limited polarization insensitivity and wide-angle stability. Recent efforts have attempted to enhance polarization robustness by increasing structural symmetry or to realize tunability by incorporating phase-change materials/graphene, but these approaches often increase structural complexity and fabrication/actuation difficulty, while it remains challenging to simultaneously achieve high absorption, high sensitivity, and wide-angle stability on a flexible platform. Overall, realizing dual-band high-absorption and high-sensitivity THz sensing with polarization- and angle-robust performance in a relatively simple and fabrication-compatible flexible design remains a topic of continuing interest.

Motivated by the above gap, we propose a dual-band THz metamaterial absorber/sensor built on a flexible PI substrate. The top layer consists of a nested outer SRR and an inner closed square ring, while a continuous metallic ground plane together with the dielectric spacer forms a metal–insulator–metal (MIM) configuration. The main contribution of this work is that, based on a simple and fabrication-compatible nested-ring MIM architecture, dual-band high-absorption sensing performance is achieved on a flexible platform while maintaining stable responses under polarization variation and oblique incidence. Full-wave electromagnetic simulations demonstrate dual-band near-perfect absorption at 1.107 THz and 1.4414 THz, and a highly sensitive, nearly linear frequency shift with refractive-index variation (maximum sensitivity up to 237.93 GHz/RIU with R^2 >0.98). Benefiting from the geometric symmetry of the unit cell and the transmission suppression inherent to the MIM configuration, the proposed device preserves stable performance over varying polarization angles and within a certain range of oblique incidence, which is more consistent with practical non-ideal illumination conditions. Furthermore, by analyzing the electric-field, magnetic-field, and surface-current distributions, we attribute the low-frequency resonance to the SRR-dominated LC mode, whereas the high-frequency resonance mainly originates from the loop-current magnetic resonance dominated by the inner square ring, confirming the relative independence of the two modes. These features enable a favorable balance among high absorption, high sensitivity, and robustness on a flexible platform, offering a feasible solution for thin-film biomolecular detection, trace chemical analysis, and wearable THz sensing applications.

2. Structural design and simulation methods

2.1. Unit cell structure design

The proposed dual-frequency terahertz metamaterial sensor adopts a classic metal-insulator-metal (MIM) structure, as shown in Fig. 1.

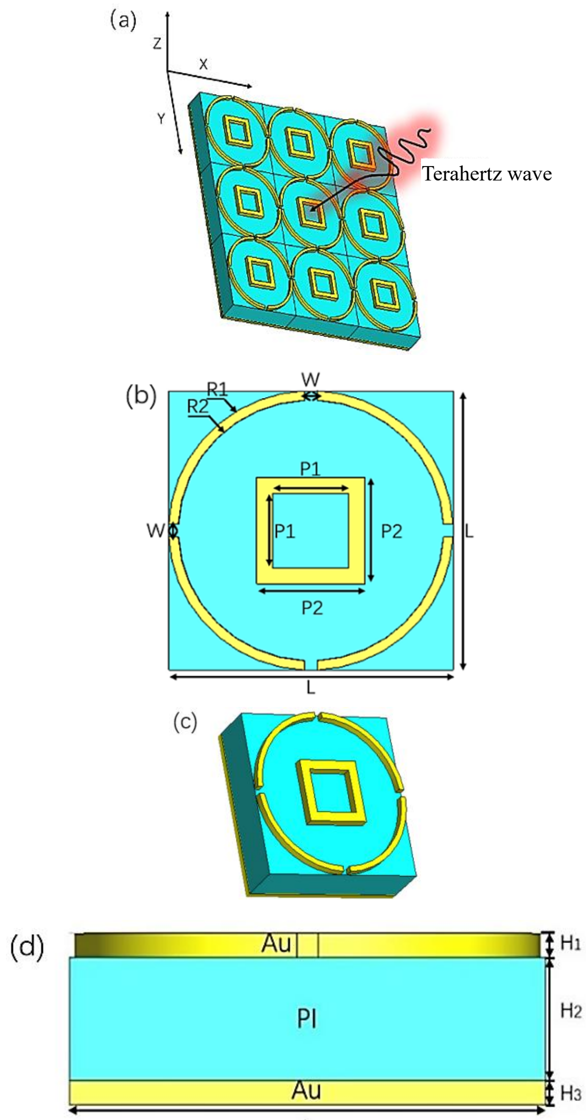

Fig. 1. Complete schematic diagram of the structure (colour online)

This structure consists of periodically arranged unit cells. The top layer is a patterned gold (Au) resonator, including an outer split-ring resonator and a nested inner square ring; the middle layer is a flexible polyimide (PI) substrate; the bottom layer is a metal Au reflective floor, which is used to block the direct transmission of THz waves and provide strong reflection. The optimized geometric parameters are listed in Table 1.

Table 1. Presents the optimized geometric parameters of the dual-frequency terahertz metamaterial sensor

parameters	L	P1	P2	H1	H2	H3	W	R1	R2
value/μm	105	28	40	0.2	6	0.6	4.8	52.5	49

The geometric parameters in Table 1 were obtained via a goal-oriented parametric sweep and physics-constrained optimization. The optimization aims to achieve dual-band high absorption in a metal–insulator–metal (MIM) architecture on a flexible PI substrate, while maintaining weak modal crosstalk and good robustness. Specifically, the outer split-ring resonator (SRR) and the inner closed square ring were first simulated separately to locate the operating bands of the low-frequency LC resonance and the high-frequency loop-current magnetic resonance, ensuring that the two resonant modes are dominated by different resonant elements. The two resonators were then nested, and the key dimensions were jointly fine-tuned under the constraint of structural symmetry to maximize the dual-band absorption and suppress inter-mode coupling. In terms of parameter roles, the SRR gap size W and the SRR scale parameters $R_1$and R_2 mainly affect the low-frequency LC resonance, whereas the square-ring parameters $P_1$and P_2 primarily determine the loop size and coupling strength of the high-frequency loop-current magnetic resonance. The period L and layer thicknesses were selected to satisfy the unit-cell approximation, suppress higher-order diffraction, and ensure that the metallic ground plane effectively blocks transmission ($S_{21} \approx 0$), thereby enabling stable near-perfect absorption.

2.2. Material parameters

Both the top-layer pattern and the bottom-layer ground plane are made of gold (Au) with an electrical conductivity of $\sigma = 4.56 \times 10^7 \, S/m$. The polyimide (PI) substrate has a relative permittivity of $\varepsilon_r = 3.5$ and a loss tangent of tanδ = 0.0027. Material selection rationale: In this design, polyimide (PI) is chosen as the dielectric substrate primarily due to its excellent mechanical flexibility and stability, which makes it suitable for conformal/wearable applications. Meanwhile, PI exhibits relatively stable dielectric properties and low loss in the terahertz band (here $\varepsilon_r = 3.5$ and $tan\delta = 0.0027$), which helps maintain sharp resonance features and sensing stability. Gold (Au) is employed for both the top resonator pattern and the bottom metallic ground plane owing to its high electrical conductivity and good chemical stability, and it is compatible with standard fabrication processes such as evaporation/sputtering. In particular, the continuous Au ground plane effectively suppresses transmission ($S_{21} \approx 0$) and, together with the PI spacer, forms a metal–insulator–metal (MIM) configuration, enabling improved impedance matching to free space and significantly reduced reflection, thereby achieving near-perfect absorption. Overall, the PI+Au material combination provides fabrication feasibility and mechanical flexibility while simultaneously supporting low-loss resonances and high absorption efficiency, making it well suited for dual-band absorber/sensor platforms. In the air environment, the dielectric constant of the upper covering layer is 1.

2.3. Simulation setup

The simulation is carried out using CST software. Periodic boundary conditions (Unit Cell) were applied along the x and y directions, while an open boundary (Open (add space)) was set along the z direction to emulate free-space radiation. The incident terahertz wave was modeled as a plane wave propagating along the $-z$ direction with the electric field polarized along the x direction by default, and it was excited via a Floquet port. The S-parameters were obtained over the frequency range of $0.1 - 2\, THz$ and used to calculate the absorption spectrum. To evaluate stability under non-ideal illumination conditions, the polarization angle $\varphi(0^0 - 90^0)$ and the oblique incidence angle $\theta(0^0 - 60^0)$ were varied while keeping the structural parameters unchanged. An adaptive tetrahedral mesh was employed, with local mesh refinement applied near metallic edges and the split gap where strong field gradients occur, to ensure accurate extraction of resonance frequencies and peak amplitudes. The convergence criterion was set to an energy error below $-40\, dB$, and the S-parameter responses were monitored to remain stable across successive adaptive iterations to guarantee the reliability and reproducibility of the results.

2.4. Performance index

The quality factor Q is employed to characterize the optical resonance performance of the sensor. A larger Q value indicates lower loss of the resonance system and a narrower resonance peak, which makes it easier to distinguish changes in the measured spectrum [16]. The Q value of the sensor can be expressed as Q = f_0/X_{FWHM}, where f_0 is the resonance frequency and X_{FWHM} is the full width at half maximum. Refractive index sensitivity S is a crucial indicator for evaluating sensor performance. A higher S value means it is easier to reflect small changes in the properties of the medium surrounding the sensor in the spectrum, and its expression is S = Δf/Δn. In this formula, Δf is the variation of the resonance frequency, Δn is the variation of the refractive index, and the unit is refractive index unit (RIU). The figure of merit (FOM) can characterize the overall performance of the sensor and enable more reasonable analysis of the sensor's performance in different frequency bands. A higher FOM value denotes better overall performance of the sensor, and its calculation formula can be expressed as $X_{FOM} = S/X_{FWHM}$. Linearity is evaluated by the R^2 value of the linear fitting between frequency shift and refractive index variation.

3. Results and discussion

3.1. Dual-band absorption characteristics

The absorption rate of the sensor can be expressed as A(ω) = 1 − R(ω) − T(ω), where ω is the frequency, R(ω) is the reflectivity, T(ω) is the transmittance, S11 is the reflection coefficient, and S_{21} is the transmission coefficient. The thickness of the metal reflective layer of the terahertz sensor designed in this paper is 0.6 μm, which is much larger than the skin depth of terahertz waves in metals. Terahertz waves cannot pass through the metal reflector, so the transmittance is almost zero, i.e., $T(\omega) \approx 0$.

In the absence of a detection sample, the absorption spectrum of the sensor under terahertz wave irradiation is shown in Fig. 2(a) and Fig. 2(b). It can be found that the structure generates two independent sharp resonance peaks at 1.107 THz (low frequency) and 1.4414 THz (high frequency), with reflection coefficients of -28.7562 dB and -27.427 dB, respectively; the absorption rates are 99.87% and 99.82%, achieving near-perfect absorption. The Q values of the sensor at low frequency and high frequency are 20.8 and 27.5, respectively; the FOM values are 4.53 and 4.3, respectively.

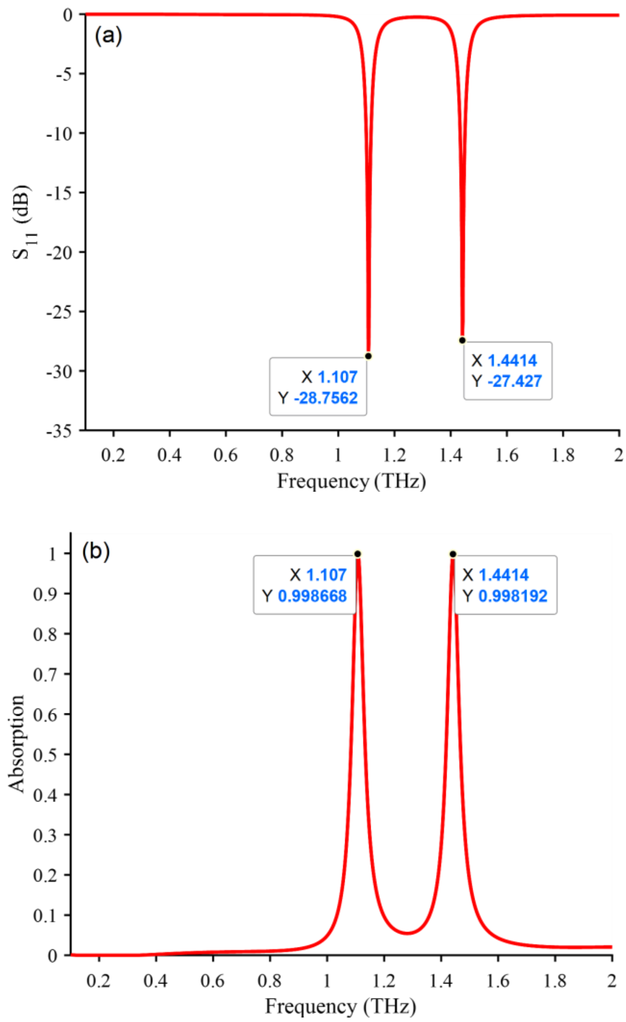

Fig. 2. Terahertz spectra of the sensor without sample. (a) Reflection coefficient; (b) Absorption rate (colour online)

3.2. Impedance-matching analysis

To further interpret the dual-band high absorption presented in Section 3.1 from an impedance-matching perspective ($S_{21} \approx 0$), the effective normalized input impedance of the absorber is retrieved from the simulated complex SSS-parameters, and its matching to free space is analyzed. For normally incident plane waves, the normalized impedance Z($Z = Z_{in}/Z_0$, where Z_0 is the free-space impedance) can be obtained via the standard S-parameter retrieval: $Z = \sqrt{\frac{(1+S_{11})^2-S_{21}^2}{(1-S_{11})^2-S_{21}^2}}$ [29]. Since the proposed device adopts a metal–insulator–metal (MIM) configuration with a sufficiently thick Au ground plane, the transmission term satisfies $S_{21} \approx 0$, and the above expression can be simplified to $Z \approx \frac{1+S_{11}}{1-S_{11}}$. According to the impedance-matching criterion, good matching to free space occurs when $R_e(Z) \approx 1$ and $I_m(Z) \approx 0$. Under this condition, reflection is strongly suppressed, leading to high absorption at the corresponding frequencies.

As shown in Fig. 3, around the two resonances the retrieved impedance exhibits $R_e(Z)$ close to 1 and $I_m(Z)$ close to 0, indicating good impedance matching to free space at $f_1 = 1.107$ THz and $f_2 = 1.4414$ THz. Consequently, reflection is significantly reduced at these frequencies, giving rise to dual-band high absorption. In contrast, away from resonance, $R_e(Z)$ and $I_m(Z)$ deviate from the matching condition, resulting in increased reflection and reduced absorption. These impedance-retrieval results quantitatively confirm that the dual-band high absorption originates from free-space impedance matching, consistent with the subsequent field and surface-current analyses of the two resonance modes.

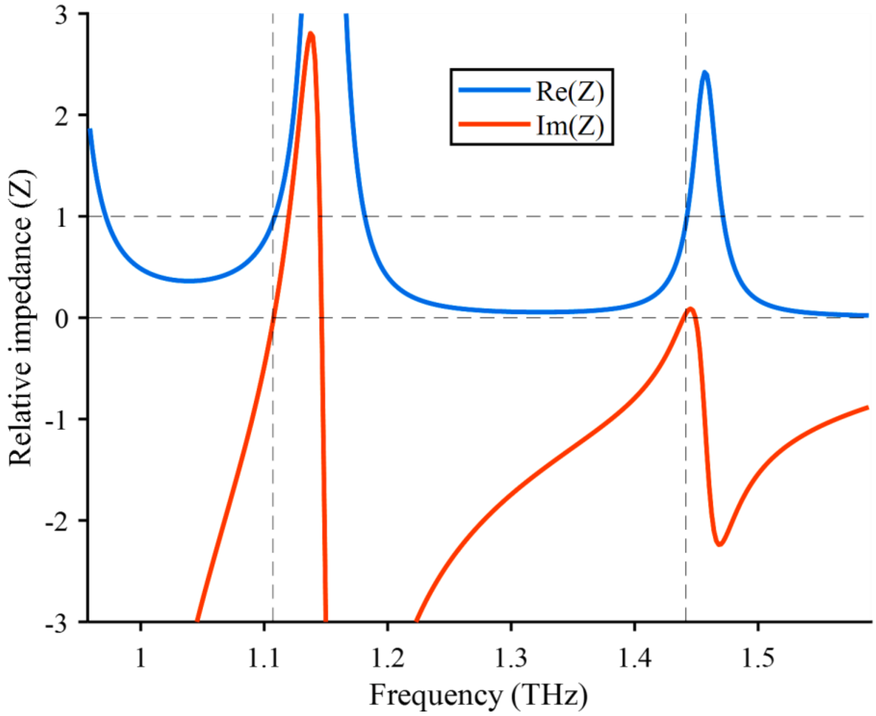

Fig. 3. Retrieved effective normalized impedance of the proposed absorber: $R_e(Z)$ and $I_m(Z)$ versus frequency. Around f_1 and f_2, $R_e(Z) \approx 1$ and $I_m(Z) \approx 0$ indicating good impedance matching to free space (colour online)

3.3. Refractive index sensing performance

To evaluate the sensing performance, an analyte layer is coated on the surface of the structure, with its refractive index set to n=1.0-1.6, and the analyte thickness fixed at $h_a = 20\mu m$. This thickness is sufficient to cover the main resonant near-field region; further increasing h_a results in only negligible additional frequency shifts, indicating that the frequency-shift response has converged. Therefore, $h_a = 20\mu m$ is adopted throughout the subsequent sensing analysis. The refractive-index range of 1.0 - 1.6 is not chosen arbitrarily; rather, it is a commonly used benchmarking interval in terahertz refractive-index sensing studies. Specifically, n=1.0 corresponds to the air background, while $n \approx 1.2 - 1.6$ covers the typical effective refractive-index range of various low-loss organic/polymer films as well as dry or low-water-content biomolecular and chemical layers in the terahertz band. The absorption spectra are shown in Fig. 4. As n increases, both resonance peaks undergo obvious red shifts, while the absorption rate remains extremely high (minimum > 98%). The relationship between resonance frequency and n is quantified by linear fitting, as depicted in Fig. 5. For the low-frequency peak, the fitting slope $S_1 = 237.93$ GHz/RIU with a linearity $R^2 = 0.9661$; for the high-frequency peak, $S_2 = 225.29$ GHz/RIU with a linearity $R^2 = 0.9861$. The sensitivity of the high-frequency mode is slightly lower than that of the low-frequency mode.

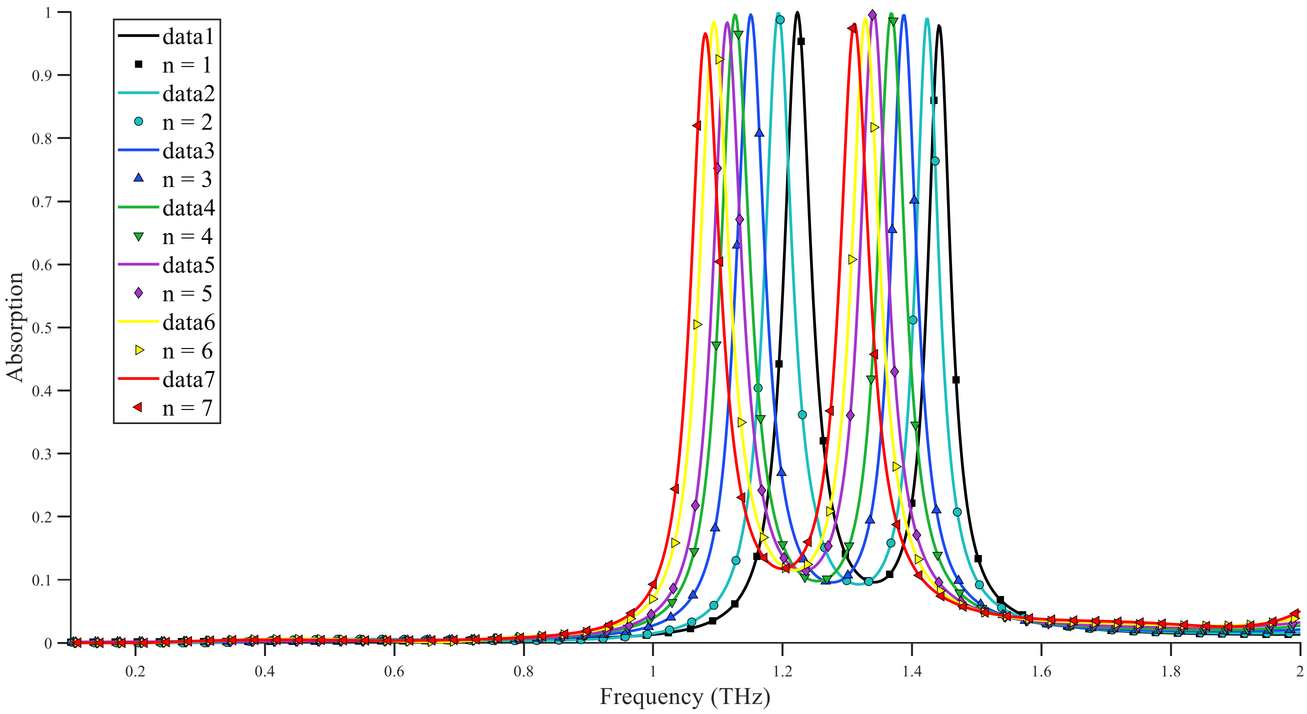

Fig. 4. Absorption spectra under different refractive indices (colour online)

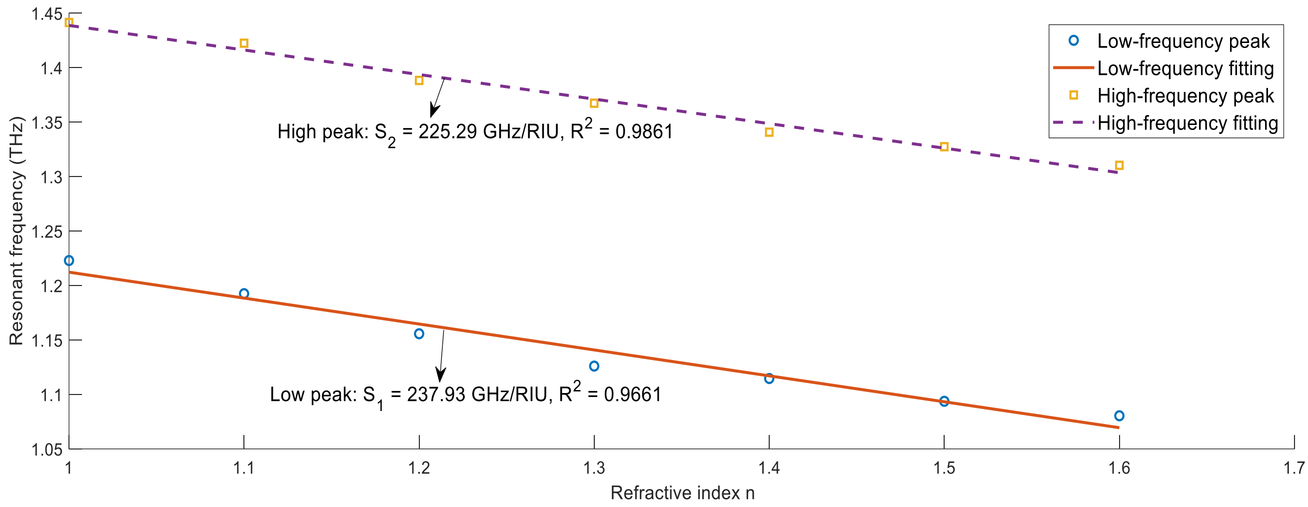

Fig. 5. Linear fitting of frequency shifts for low and high resonance peaks (colour online)

The sensitivity of the high-frequency mode is slightly lower than that of the low-frequency mode. The low-frequency sensitivity of the absorber designed in this paper (237 GHz/RIU) is at a relatively high level, and the high-frequency sensitivity is also competitive. The excellent linearity ($R^2 > 0.98$) facilitates quantitative detection, and the absorption rate remains stable over a wide refractive index range, which is superior to the absorption attenuation with increasing n observed in many reported designs. The independent responses of the dual modes support multi-analyte detection or self-referenced measurement, further enhancing the practicality of the sensor.

3.4. Polarization and angular stability

In practical applications, the polarization and angle of incident waves are often non-ideal. To verify the robustness of the sensor, the variation of polarization angle $\emptyset$ from 0° to 90° (step size 15°) is first simulated. The absorption spectra are shown in Fig. 6, where (a) and (b) represent the reflection coefficient and absorption rate under incident waves with different polarization angles, respectively. All curves of the high-frequency peak and low-frequency peak almost completely overlap, showing excellent polarization insensitivity. The polarization insensitivity of the sensor originates from the high symmetry of the surface structure.

Then, the influence of oblique incidence angle θ from 0° to 60° (step size 10°) is investigated, as shown in Fig. 6, where (c) and (d) represent the reflection coefficient and absorption rate under different oblique incidence angles, respectively. When θ ≤ 50°, the absorption rates of both peaks are greater than 90% (most > 98%); only when θ = 60°, the absorption rate of the low-frequency peak decreases to about 84%, accompanied by a slight peak red shift and broadening. This wide-angle stability is superior to many dual-frequency designs, benefiting from the robust impedance matching of the MIM structure and symmetric resonator. Synthesizing the polarization and angular stability results, the sensor still maintains reliable performance under complex incident conditions (random polarization and oblique incidence).

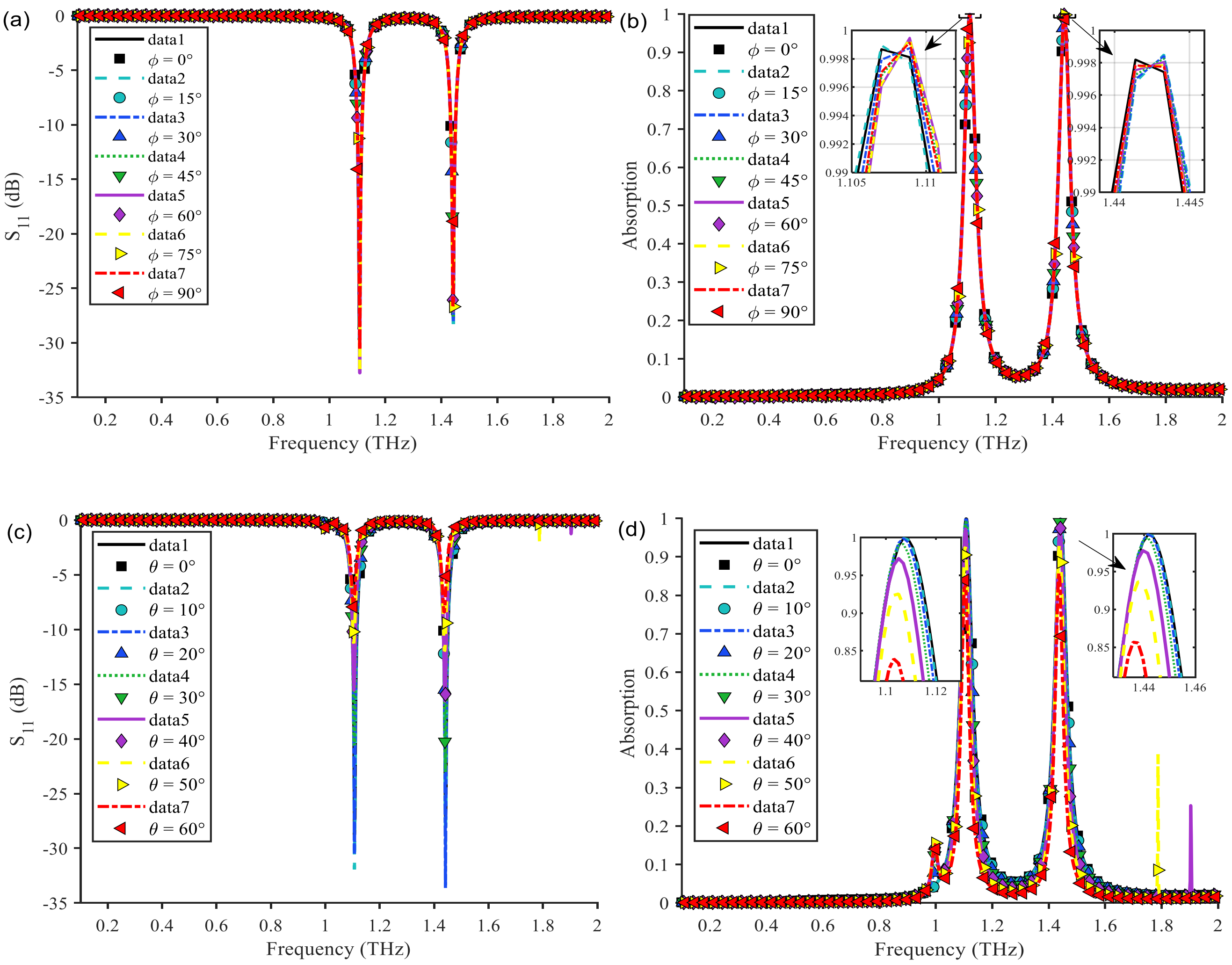

Fig. 6. Polarization and angular stability of the proposed sensor. (a) Reflection coefficient $|S_{11}|(dB)$ under different polarization angles $\varphi = 0^0 - 90^0$ (step 15^0) at normal incidence; (b) Corresponding absorption spectra A; (c) $|S_{11}|(dB)$ under oblique incidence angles $\theta = 0^0 - 60^0$(step 10^0) for TE-polarized incidence; (d) Corresponding absorption spectra A (colour online)

3.5. Physical mechanism analysis

To clarify the origin of dual frequencies and the independence of resonance between the inner and outer rings, the field distribution and surface current distribution are extracted at the resonance frequencies. Meanwhile, to further verify the mode independence, the absorption spectra of the isolated inner ring and isolated outer ring structures are simulated, as shown in Fig. 7(a) and (b) are the absorption rate curves of the single ring and single square ring, respectively; Fig. 7(c) shows the comparison of absorption rate curves between the single ring, single square ring and the complete resonant layer structure. From the simulation results, it can be concluded that the isolated outer ring generates a single low-frequency peak, and the isolated inner ring generates a single high-frequency peak, with both absorption rates reaching more than 99%, indicating that they are separate and independent resonances. The positions of the two peaks in the complete nested structure are highly consistent with those of the isolated structures.

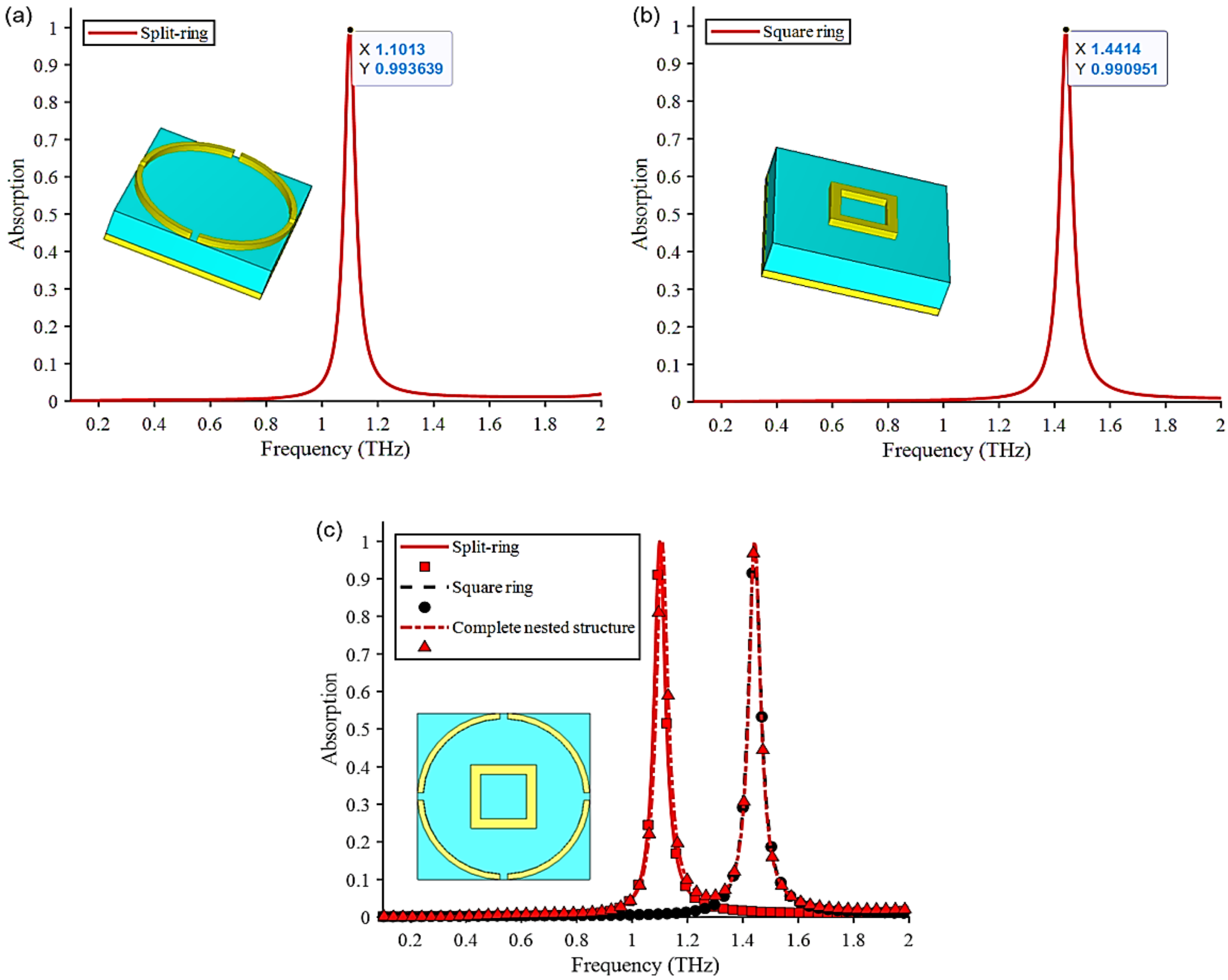

Fig. 7. Verification of resonance-mode independence. (a) Absorption spectrum of the outer split-ring resonator (SRR) only; (b) Absorption spectrum of the inner closed square ring only; (c) Comparison of absorption spectra among the SRR-only structure, the square-ring-only structure, and the complete nested structure (colour online)

The electric field E distribution is shown in Fig. 8, at the low-frequency mode (1.107 THz), the field is mainly localized on the side of the outer ring (high-intensity region), and the inner ring is weakly involved; at the high-frequency mode (1.4414 THz), the field is strongly concentrated on the edges of the inner closed square ring, while the field of the outer ring is weak. This result indicates that the low-frequency mode is an outer ring-dominated mode with capacitance as the main factor, and the high-frequency mode is a resonance dominated by the inner ring.

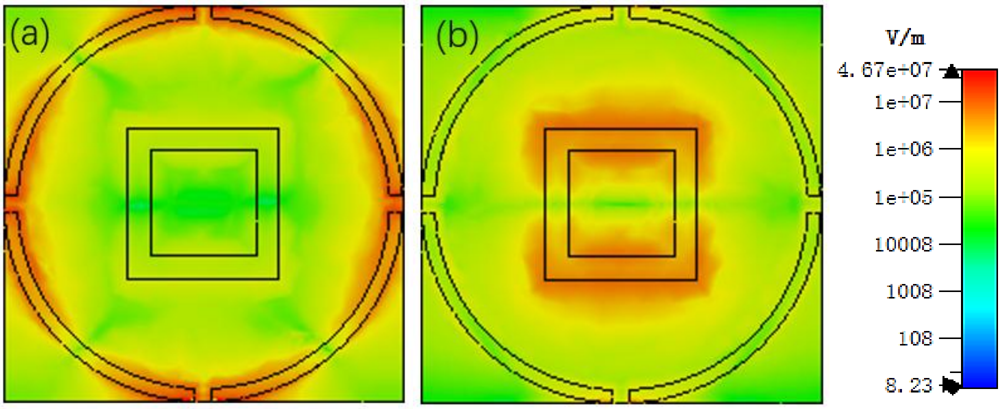

Fig. 8. Electric-field intensity distributions at the two resonances under TE-polarized normal incidence (E): (a) f=1.107 THz; (b) 1.4414 THz (colour online)

The magnetic field H distribution is shown in Fig. 9. For the low-frequency mode, the magnetic field is strongly enhanced inside the outer ring, forming an annular magnetic dipole; for the high-frequency mode, the magnetic field shifts to the inside of the inner ring, showing more compact localization.

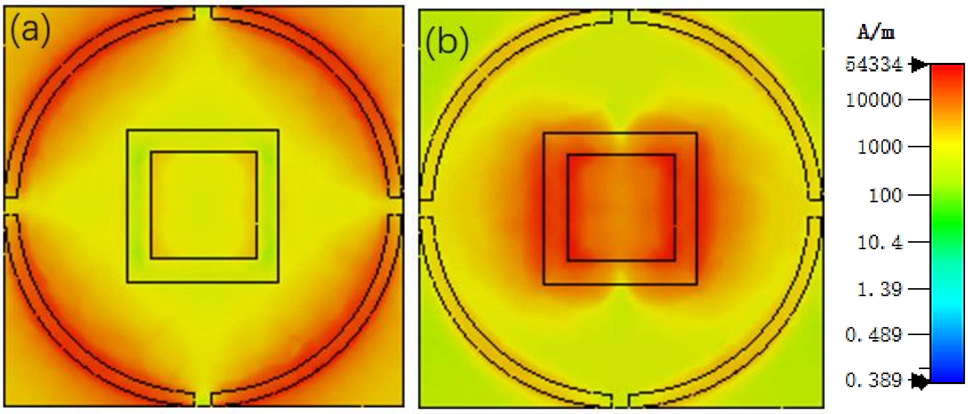

Fig. 9. Magnetic-field intensity distributions at the two resonances under TE-polarized normal incidence. (H): (a) f = 1.107 THz; (b) f = 1.4414THz (colour online)

The electric field distribution diagrams under TM mode are shown in Fig. 10: (a) and (b) correspond to the low frequency (f = 1.107 THz) and high frequency (f = 1.4414 THz), respectively. These distributions are only rotated by 90° compared with those under TE polarized incidence, indicating that the sensor has prominent polarization independence.

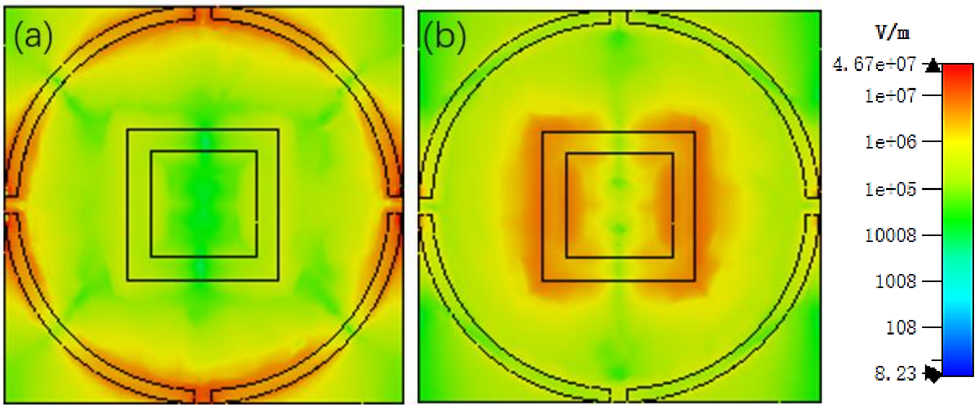

Fig. 10. Electric-field intensity distributions under TM-polarized normal incidence (E): (a) TM mode at f = 1.107 THz; (b) TM mode at f = 1.4414 THz (colour online)

The surface current diagrams of the resonant layer are shown in Fig. 11 (a), (b), (c), and (d). The opposite current directions in the left and right half-rings of this surface current distribution are a typical characteristic of the nested symmetric structure. The opposite-direction circular currents suppress net dipole radiation, leading to high energy trapping and near-perfect absorption. Current symmetry enhances the local field, ensures mode independence, and reduces cross-coupling between the inner and outer rings. At low frequencies, the current flows along the split ring and accumulates at the split; at high frequencies, the current is strongly distributed along the four sides of the square ring. This indicates that the low frequency is dominated by the split ring, the high frequency is dominated by the square ring, and the two peaks are clearly separated. The symmetric distribution reduces sensitivity to polarization and angle. Overall, this current configuration optimizes comprehensive performance, making the device more practical and suitable for thin-layer biomolecular detection.

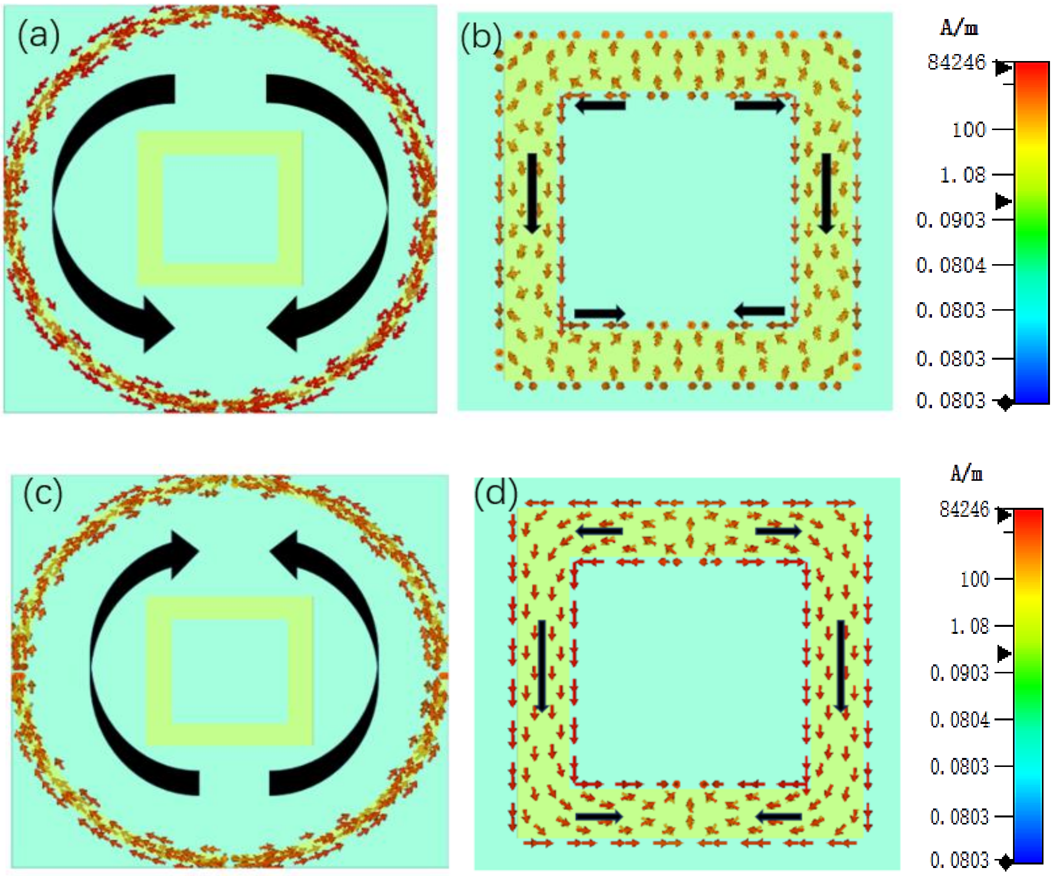

Fig. 11. Surface current distributions on the split-ring resonator and the square ring at the two resonances. (a) Split ring at f = 1.107 THz; (b) Square ring at f = 1.107 THz; (c) Split ring at f = 1.4414 THz; (d) Square ring at f = 1.4414 THz (colour online)

3.6. Fabrication tolerance and experimental feasibility

The proposed device is composed of metallic patterns and a continuous ground plane on a flexible PI substrate. The micrometer-scale geometries are compatible with standard micro and nano-fabrication processes. The top metallic pattern can be realized via photolithography/laser direct writing or electron-beam lithography combined with metal deposition and lift-off, while PI has a mature flexible fabrication foundation. Considering inevitable dimensional deviations (±3–5%), the high symmetry of the unit cell and the fact that the two resonances are primarily dominated by separate resonators ensure that small geometric perturbations only induce minor shifts in resonance frequencies without destroying the dual-peak features or overall absorption performance, providing sufficient fabrication tolerance.

For experimental verification, the thick metallic ground plane suppresses transmission, so absorption can be approximated from the reflection spectrum. THz time-domain spectroscopy (THz-TDS) in reflection mode or continuous-wave THz reflection measurements can be employed to obtain S11 and derive the absorption spectrum. Polarization and oblique-incidence stability can be evaluated by rotating a polarizer and adjusting the sample angle. For sensing tests, thin analyte layers can be deposited (drop-cast, spin-coated, or using microfluidic thin-layer chambers) to create different refractive-index environments and verify the linear relationship between resonance shifts and refractive-index variations, as well as the sensitivity.

To verify the superiority of the sensor designed in this paper, a comparison with other literatures is conducted. Table 2 summarizes the performance comparison of dual-band terahertz metamaterial sensors reported in recent literatures.

Table 2. Performance comparison between this work and other literatures

Literatures	Sensitivity S (GHz/RIU)	Q	FOM (RIU^{-1})
[21]	1215	65.8	21.5
[22]	151	54.5	12.6
[23]	243	14.2	3.3
[24]	39.5, 85	28.1,29.3	2.86, 3.58
Proposed	237, 225	20.8, 27.5	4.53, 4.3

In this study, the low-frequency sensitivity of 237 GHz/RIU is at a relatively high level, which is not only significantly superior to that of the dual-band sensor in Reference [24] (39.5 GHz/RIU and 85 GHz/RIU) but also close to the 243 GHz/RIU of the single-band sensor in Reference [23], while the high-frequency sensitivity also exhibits strong competitiveness [23, 24]. Compared with the single-band high-sensitivity sensor (1215 GHz/RIU) in Reference [21], although there is a gap in the sensitivity of a single frequency band, the proposed design can meet the demand for simultaneous detection of multiple analytes by virtue of its dual-band characteristics. Moreover, it possesses the advantage of flexibility, making up for the application limitations of single-band sensors [21]. In addition, the excellent linearity ($R^2 > 0.98$) facilitates quantitative detection, and the absorption rate remains stable over a wide range of refractive index (n), which is superior to the attenuation of absorption rate with n in many designs. The independent response of the dual modes supports the detection of multiple analytes or self-reference measurement, further enhancing the practicality of the sensor.

4. Conclusion

This paper proposes and simulates a dual-band terahertz metamaterial sensor based on a flexible polyimide (PI) substrate, consisting of nested split rings and closed square rings. By optimizing the metal-insulator-metal (MIM) structure, two independent resonance peaks at 1.107 THz and 1.4414 THz are achieved in an air environment, with absorption rates reaching 99.87% and 99.82%, respectively. The Q-factor of the low-frequency mode is 20.8, with a refractive index sensitivity of approximately 237 GHz/RIU; the high-frequency mode has a Q-factor of 27.5 and an ultra-high sensitivity of 225 GHz/RIU. Additionally, the frequency shift exhibits an excellent linear relationship with the change in refractive index ($R^2 > 0.98$). The designed sensor demonstrates outstanding polarization insensitivity (absorption spectra almost overlap within the polarization angle range of 0°−90°) and angular stability (absorption rate > 90% at an oblique incidence angle of up to 50°, and > 83% at 60°).

Analysis of the electromagnetic field and surface current distributions clearly reveals the dual-band mechanism: the low-frequency peak is excited by the fundamental LC resonance dominated by the outer split ring, with currents forming split circulations in opposite directions in the left and right half-rings; the high-frequency peak is generated by the circular current magnetic resonance dominated by the inner closed square ring, where the currents also form split circulations in opposite directions in the left and right half-rings. This symmetric split circulation (anti-parallel currents) suppresses net radiation, enhances field localization, achieves independent separation of modes and high absorption, while improving surface sensitivity and environmental robustness.

Compared with recent dual-band terahertz metamaterial sensors, this work simultaneously achieves near-perfect absorption, high sensitivity, and polarization/angle insensitivity on a flexible substrate. Moreover, it features a simple structure, easy processing, and no need for auxiliary active materials. The sensor is particularly suitable for thin-layer biomolecular detection, chemical trace identification, as well as wearable and conformable label-free sensing scenarios. Its dual-mode characteristic also supports simultaneous detection of multiple analytes or self-reference measurement. Future work can focus on experimental fabrication and verification (including photolithographic processing and THz time-domain spectroscopy testing), simulation of specific detection of thin-layer biomolecules (such as proteins and DNA), and further optimization of Q-factor and sensitivity through fine-tuning of geometric parameters. This design provides an effective reference for the development of flexible and highly robust terahertz sensing platforms.

References

[1] J. Yu, H. Pu, D. W. Sun, Chemical Engineering Journal **520**, 166006 (2025).
[2] S. Guo, C. Li, D. Wang, W. Chen, S. Gao, G. Wu, J. Xiong, Applied Optics **63**, 1962 (2024).
[3] G. Liu, Z. Sun, J. Liu, Y. Du, Physics Letters A **558**, 130906 (2025).
[4] A. Alqurashi, S. Khanam, E. Y. O. Zafar, A. J. A.

Al-Gubri, Results in Optics **21**, 100917 (2025).
[5] X. Liu, J. Sun, Z. Shi, C. Yang, Y. Hou, L. Zhang, S. Xiu, IEEE Sensors Journal **25**(12), 21520 (2025).
[6] Y. I. Abdulkarim, O. Altintas, A. S. Karim, H. N. Awl, F. F. Muhammadsharif, F. O. Alkurt, M. Bakir, B. Appasani, M. Karaaslan, J. Dong, ACS Omega **7**(42), 38094 (2022).
[7] X. Lu, H. Ge, Y. Jiang, Y. Zhang, Frontiers in Physics **10**, 973033 (2022).
[8] S. J. Mishu, M. A. Rahman, N. Dhar, Heliyon **10**(5), e26842 (2024).
[9] M. Cui, G. Zhang, K. Bi, B. Xing, G. Diao, Y. Du, Z. Ge, Y. Zhang, Physics Letters A **552**, 130632 (2025).
[10] K. Aliqab, A. Armghan, M. Alsharari, Scientific Reports **14**, 19149 (2024).
[11] Yuying Lu, Jining Li, Shaohua Zhang, Jinhai Sun, Jian Quan Yao, Applied Optics **57**, 6269 (2018)
[12] Garima Tiwari, Pramod Kumar Gupta, Trivesh Kumar, Biswajeet Mukherjee, Physica Scripta **100**(7), 075501 (2025).
[13] Vijayalakshmi Kannaiyan, Physica Scripta **100**(12), 125501 (2025).
[14] Tingting Lang, Jinhui Zhang, Yanqing Qiu, Zhi Hong, J. Liu, Optics Communications **537**(2), 129430 (2023).
[15] Z. Dai, C. Yan, Y. Ye, M. Chen, Y. Liang, J. Li, Optics Express **32**, 35030 (2024).
[16] D. Wang, K. D. Xu, 2023 IEEE MTT-S International Wireless Symposium (IWS), pp. 1-3 (2023).
[17] S. Nourinovin, S. J. Park, Q. H. Abbasi, A. Alomainy EPJ Applied Metamaterials **10**, 4 (2023).
[18] Tao Chen, Dapeng Zhang, Fengyu Huang, Zhi Li, Fangrong Hu, Materials Research Express **7**(9), 095801 (2020).
[19] M. A. Khalil, W. H. Yong, T. Batool, A. Hoque, L. Y. Chiong, H. H. Goh, T. A. Kurniawan, M. S. Soliman, M. T. Islam, Scientific Reports **15**, 2283 (2025).
[20] L. Cao, S. Jia, F. Meng, M. Richter, Y. Loth, A. K. Wigger, C. Yang, L. Zhang, P. H. Bolívar, H. G. Roskos, Advanced Materials Technologies **10**(9), 2401358 (2025).
[21] A. Teber, Turkish Journal of Nature and Science, **13**(2), 61 (2024).
[22] C. Wei, H. Sun, X. Wang, Appl. Opt. **64**(22), 6419 (2025).
[23] Z. Wang, Z. Geng, W. Fang, Optics Express **28**(18), 26370 (2020).
[24] H. Z. Pang, X. Wang, J. L. Wang, Z. L. Wang, S. Y. Liu, H. Q. Tian, Acta Physica Sinica **70**(16), 168101 (2021).
[25] L. Li, F. Chen, W. Yang, Y. Zao, Micro and Nanostructures **209**, 208408 (2026).
[26] Y. Li, F. Chen, W. A. Yang, Optics Communications **586**, 131878 (2025).
[27] L. Li, F. Chen, Physics Letters A **544**, 130489 (2025).
[28] Y. Pan, Q. Meng, F. Chen, S. Cheng, W. Yang, D. Yao, Z. Yi, Optics Communications **540**, 129486 (2023).
[29] H. Fu, F. Chen, Physics Letters A **574**, 131395 (2026).

*Corresponding author: liujianjun8888@hotmail.com; 287370018@qq.com